



Contents lists available at ScienceDirect

Journal of Power Sources

journal homepage: www.elsevier.com/locate/jpowsour

Branched hierarchical photoanode of titanium dioxide nanoneedles on tin dioxide nanofiber network for high performance dye-sensitized solar cells

Caitian Gao^a, Xiaodong Li^{b,*}, Xupeng Zhu^c, Lulu Chen^a, Zemin Zhang^a, Youqing Wang^a, Zhenxing Zhang^a, Huigao Duan^c, Erqing Xie^{a,*}

^a School of Physical Science and Technology, Lanzhou University, Lanzhou 730000, Gansu, PR China

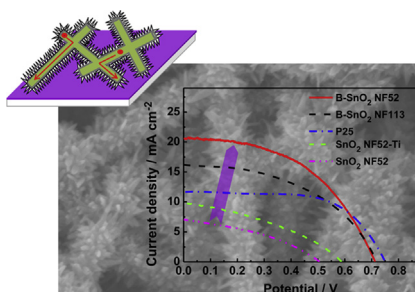
^b New Materials R&D Center, Institute of Chemical Materials, China Academy of Engineering Physics, Mianyang 621900, Sichuan, PR China

^c Key Laboratory for Micro-Nano Optoelectronic Devices of Ministry of Education, Hunan University, Changsha 410000, Hunan, PR China

HIGHLIGHTS

- SnO_2 – TiO_2 branched nanostructure serves as model architecture for DSSCs.
- The novel structure combines fast electron transport, slow recombination and high specific surface area.
- A maximum efficiency of 7.06% was achieved.

GRAPHICAL ABSTRACT



ARTICLE INFO

Article history:

Received 21 January 2014

Received in revised form

31 March 2014

Accepted 13 April 2014

Available online 24 April 2014

Keywords:

Dye-sensitized solar cells

Electrospinning

Tin dioxide nanofiber network

Core–shell

Fast electron transport

Slow recombination

ABSTRACT

We report a branched hierarchical nanostructure of TiO_2 nanoneedles on SnO_2 nanofiber network (B- SnO_2 NF) that serves as model architecture for highly efficient dye-sensitized solar cells (DSSCs). The nanostructure simultaneously offers a low degree of charge recombination, a fast electron transport and a large specific surface area. The power conversion efficiency for B- SnO_2 NF52 (with SnO_2 NF diameter ~ 52 nm) is up to 7.06%, increased by 26% and 40% compared to B- SnO_2 NF113 (5.57%, with SnO_2 NF diameter ~ 113 nm) and TiO_2 nanoparticle (5.04%, P25), respectively, and more than five times as large as SnO_2 NF52 (1.34%). The distinct photovoltaic behavior of the B- SnO_2 NF52 is its large short-circuit current density (J_{sc} , 20.5 mA cm^{-2}) as compared with the commonly used P25 photoanode (11.7 mA cm^{-2}). Our results indicate that J_{sc} enhancement derived by the slower electron recombination associated with the SnO_2 – TiO_2 core–shell heterojunction and faster electron transport in SnO_2 NF network could synergistically contribute to high efficiency.

© 2014 Elsevier B.V. All rights reserved.

1. Introduction

Dye-sensitized solar cells (DSSCs), a promising alternative for the development of a new generation of photovoltaic devices, are a successful combination of materials, which typically consists of a transparent conducting electrode coated with a dye-sensitized metal oxide film, an electrolyte containing a suitable redox-

* Corresponding authors. Fax: +86 931 8913554.

E-mail addresses: lixd04@163.com, lixdong10@gmail.com (X. Li), xieeq@lzu.edu.cn (E. Xie).

couple and a Pt coated counter electrode [1–5]. Nanostructured metal oxides are one of key factors in determining the power conversion efficiency (PCE) of DSSCs, because they are related to the dye loading, light scattering, electrolyte penetrating, electron injection, transport and recombination. Early efforts focused on the development of TiO_2 nanoparticle (NP) films [1,6–10] due to their large surface area to volume ratios. However, the TiO_2 NP films suffer from high charge recombination loss owing to the numerous grain boundaries existing in the nanoparticle film and the slower electron mobility of TiO_2 as compared with other materials such as SnO_2 [11–16], ZnO [17–19], and BaSnO_3 [20–22]. In recent years, one-dimensional (1D) nanostructures have attracted significant attention for applications in DSSCs due to their enhanced charge collection efficiency in terms of speeding up electron transport and slowing recombination as compared to the NP films [18,19,23–28]. However, in the present state-of-the-art research, these 1D structures usually increase the charge collection efficiency at the expense of specific surface area, resulting in a low PCE.

An efficient way to achieve fast electron transport and slow recombination is to use the SnO_2 – TiO_2 core–shell structured photoanodes in DSSCs. SnO_2 is a good alternative of TiO_2 in DSSCs due to its higher electron mobility (~ 100 – $200 \text{ cm}^2 \text{ V}^{-1} \text{ s}^{-1}$) [29] than that of TiO_2 (~ 0.1 – $1.0 \text{ cm}^2 \text{ V}^{-1} \text{ s}^{-1}$) [30], indicating a faster diffusion transport of photoinduced electrons in SnO_2 than in TiO_2 . However, the essential drawbacks of the SnO_2 -based DSSCs are a 300 mV positive shift of the conduction-band edge of SnO_2 with respect to that of TiO_2 , which hence results in faster interfacial electron recombination and lower trapping density [11,31], as well as less adsorption of the dyes with acidic carboxyl groups due to the lower isoelectric point [23,32]. Bridging the gap between SnO_2 and TiO_2 is combination of the advantageous features of the two materials by using SnO_2 – TiO_2 core–shell structured DSSCs. Recently, various morphologies of SnO_2 , including multilayered hollow microspheres [11], nanotubes [15,33], nanoparticles [34,35], have been synthesized and exhibited interesting photovoltaic performance in SnO_2 – TiO_2 core–shell DSSC applications, for which a conversion efficiency of around 4.97–5.78% is reported [11,14,15,36].

On the other hand, as compared with other methods for preparation of 1D nanomaterials, electrospinning offers the most straightforward and cost-effective approach to generate various 1D nanomaterials with high aspect ratios and specific surface areas, including nanofibers [37], nanotubes [15], and nanobelts [38]. The electrospun 1D nanostructures, such as nanofibers and nanotubes, can provide a direct pathway for electron transport and large surface area for dye loading at the same time.

In this work, we fabricated SnO_2 nanofibers with thin diameters $\sim 52.4 \text{ nm}$, which were coated on fluorine-doped SnO_2 (FTO) glass followed by solution heteroepitaxial growth of TiO_2 nanoneedles to form SnO_2 – TiO_2 core–shell photoanode (B- SnO_2 NF52). As compared to the previous reports of SnO_2 – TiO_2 DSSCs with different photoanode architectures [14,16,28,33], the advancement of this work is: (1) the 1D SnO_2 NF network was constructed on FTO layer prior to the TiO_2 shell growth, which is obviously advantageous in electron transport because that happens within only SnO_2 NF network; (2) the large pores resulted from the stacking of 1D SnO_2 NFs are beneficial to the complete penetration of the reaction solution and ideal coating of TiO_2 shell, generating an effective core–shell structure; and (3) the electrospun SnO_2 NF with thinner diameter and the needle-like TiO_2 layer provide a large specific surface area for dye loading. Therefore, this branched hierarchical core–shell nanostructure simultaneously offers a low degree of charge recombination, a fast electron transport and a large specific surface area. By N-719 sensitizing, the B- SnO_2 NF52 based DSSC generates a large enhancement in short-circuit current density (J_{sc} ,

20.52 mA cm^{-2}) compared with the commonly used P25 photoanode (11.67 mA cm^{-2}), and thus a high PCE of 7.06%.

2. Experimental section

2.1. Preparation of the thin SnO_2 NF

To prepare the precursors for electrospinning, certain amounts of tin dichloride dihydrate ($\text{SnCl}_2 \cdot 2\text{H}_2\text{O}$, Tianjin Chemical Corp., China) and polyvinyl pyrrolidone (PVP, Sigma Aldrich, $M_w \approx 1\,300\,000$) (weight ratio of 1:1.33) were dissolved in a mixture of ethanol (2.2 g) and N,N-dimethyl formamide (2.2 g) by magnetic stirring for 1 h. The concentration of PVP and SnCl_2 in the solution was varied from 13.7 to 10.6 and 7.3 wt.% to generate fine SnO_2 nanofibers. The applied voltage and the distance between the syringe needle and the collector were fixed at 13.5 kV and 15 cm, respectively. The solution feeding rate was 0.1 mL h^{-1} . The composite fibers in the form of non-woven mats were collected and annealed at 500°C for 2 h with a heating rate of $3.5^\circ\text{C min}^{-1}$ in air.

2.2. Preparation of the branched photoanodes

To obtain the branched SnO_2 NF– TiO_2 (B- SnO_2 NF) photoanodes, the annealed nanofibers (0.08 g) were ultrasonically dispersed in a mixture of acetic acid (1.5 mL), deionized water (0.4 mL) and ethanol (0.1 mL) for 10 min. Then polyethylene glycol ($M_w \sim 20,000$, 0.02 g) was added to the above solution and stirred for 30 min. The resultant paste was coated on FTO glass substrates (2.2 mm in thickness, >80% transmittance, 7Ω per square, Nippon, Japan) by drop-drying method. The films were then sintered at 500°C for 30 min in air. The thickness of all the SnO_2 NF based films was fixed at $\sim 6 \mu\text{m}$.

For the synthesis of the branches, the annealed SnO_2 NF films were immersed in a brown glass bottle with an aqueous solution [39] consisting of DI water (10 mL), HCl (0.1 mL), and TiCl_3 solution (0.1 mL, 20 wt. % of TiCl_3 in H_2O and HCl solution, Sinopharm Chemical Reagent Co., Ltd., Shanghai, China), and then kept at certain temperatures for 40 min in an oil-bath heater. The temperature greatly affected the growth of the TiO_2 nanoneedles on SnO_2 NF, and 75°C is an optimum growth condition in this study, as shown in Fig. S1, Supporting information. At last, the samples were successively washed with deionized water and ethanol and subsequently annealed at 450°C for 1 h in air.

2.3. Assembling of DSSCs

The details of fabrication of the TiO_2 nanoparticle (P25) film and assembling process of the DSSCs have been described in our previous works [15,19].

2.4. Characterizations

The morphology and structure of the samples were characterized by field emission scanning electron microscopy (FE-SEM, Hitachi S-4800) and transmission electron microscopy (TEM, FEI Tecnai F30). X-ray diffraction (XRD, Philips, X'pert pro, $\text{Cu K}\alpha$, 0.154056 nm) was employed to characterize the structural properties of the samples. Raman scattering spectra were carried out on a Jobin-Yvon LabRam HR80 spectrometer (with a 532 nm line of Torus 50 mW diode-pumped solid-state laser) under the backscattering geometry at room temperature. The film thicknesses were obtained by using a surface profile measurement system (Veeco, Dektak8 ADP-8). The amount of adsorbed dye was determined by UV–VIS absorption measurement (TU-1901) of the chemically desorbed N719 solution using the absorption peak

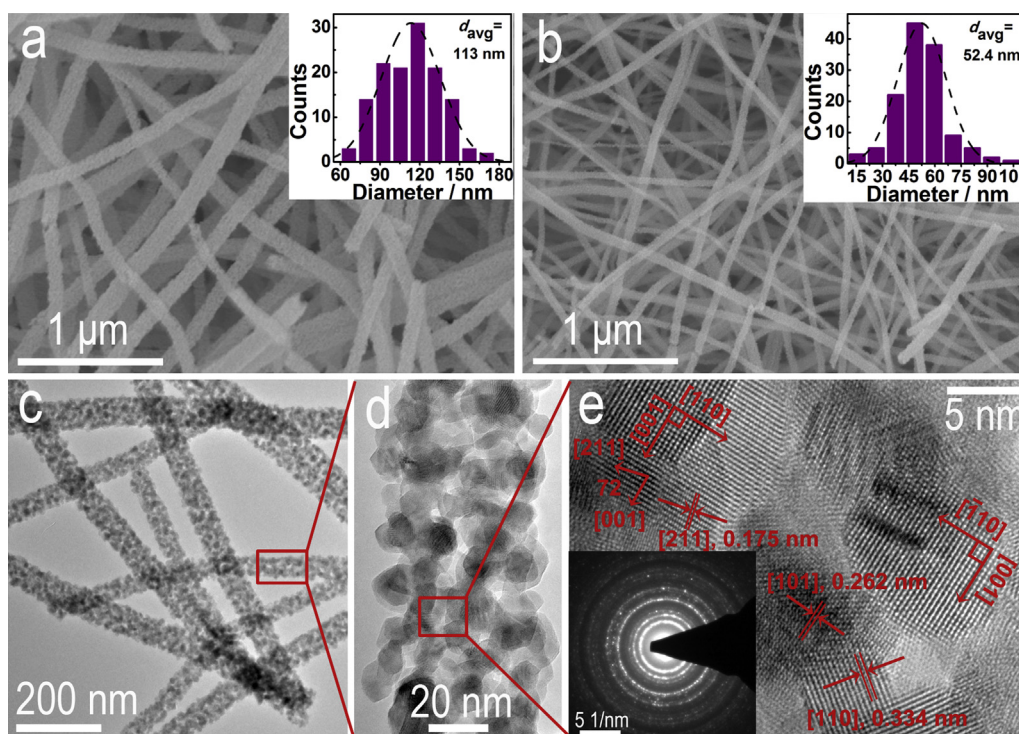


Fig. 1. FE-SEM images of the SnO_2 nanofibers fabricated from precursors with the concentration of PVP and SnCl_2 of 13.7 (a) and 10.6 wt.% (b). Inset shows the corresponding diameter distribution. (c) and (d) are TEM images of the nanofibers fabricated from 10.6 wt.% PVP and SnCl_2 (denote as SnO_2 NF52). HRTEM image (e) and SAED pattern (inset) taken from the area selected in Fig. 1e.

intensity of N719 at 515 nm. The adsorbed dye was chemically desorbed in a 0.1 M solution of NaOH in a mixture of EtOH/ H_2O (volume ratio of 1:1). Photovoltaic performance and electrochemical impedance spectroscopy (EIS) of the devices were obtained on an Electrochemical Workstation (RST5200, Zhengzhou Shiruishi Instrument Technology Co., Ltd., China). EIS measurements were carried out in the frequency range of 0.01 Hz–100 kHz at open-circuit voltage with a potential pulse of 10 mV in amplitude.

3. Results and discussion

In electrospinning process, it is argued that low polymer concentration has more solvent to evaporate and hence takes longer to solidify, which generates nanofibers with thinner diameter. Therefore, in order to obtain thinner SnO_2 nanofibers with regular 1D structures, we varied the concentration of PVP and SnCl_2 in the solution from 13.7 to 10.6 and 7.3 wt.% with a fixed PVP/ SnCl_2 weight ratio of 1.33, and the FE-SEM images of the respective samples are shown in Fig. 1 and Fig. S2. As the concentration decreased from 13.7 wt.% to 10.6 wt.%, nanofibers with an average diameter of about 113 nm (Fig. 1a) changed into thinner nanofibers with an average diameter of about 52.4 nm (Fig. 1b). With further decrease the concentration to 7.3 wt.%, nanofibers of ~ 45 nm in average diameter with beads along them were produced (Fig. S2).

From the TEM image shown in Fig. 1c and d, it can be seen that the SnO_2 NFs formed from numerous primary nanoparticles ~ 12.5 nm in diameter. The high resolution TEM (HR-TEM) image and selected area electron diffraction (SAED) pattern are shown in Fig. 1e, revealing the polycrystalline nature of the nanofibers, and the patterns could be indexed to the rutile SnO_2 (JCPDS no. 41-1445). The SnO_2 NFs reported here, compared to NFs from previous

reports, have smaller diameters, leading to larger surface to volume ratios, a desired feature for DSSCs applications.

The preparation of B- SnO_2 NF on FTO is illustrated in Fig. 2. The SnO_2 NF network was fabricated on FTO by drop-drying method using a SnO_2 NF paste described in Experimental section. As shown in Fig. 3a, the continuous fibers were cut into nanowires with an average length of ~ 1.2 μm and an average aspect ratio of 20 upon ultrasonic dispersion. The resulting SnO_2 NFs were dispersed homogeneously over a large area without aggregates, as shown in Fig. 3a.

The growth of TiO_2 branches causes tensile stress in the SnO_2 NF network, which can lead to the occurrence of cracks in the SnO_2 NF network and even peeling off of the SnO_2 NF network from the FTO substrate. Therefore, prior to growth of TiO_2 branches, a layer of TiO_2 was coated on the SnO_2 NF network. We found that this layer (~ 2 nm, see Fig. 3c) was vital to stabilizing the SnO_2 NF network as well as preventing cracking and peeling off of the SnO_2 NF network from the substrate in subsequent growth of TiO_2 branches. By coating of the thin TiO_2 layer, it is sufficient to fabricate 6 μm -thick B- SnO_2 NF film on FTO without peeling off.

After growth of the branches by directly dipping the SnO_2 film into a TiCl_3 aqueous solution, the diameter of the SnO_2 NFs increased, but their macroscopic porous morphology was retained. The typical morphology of the B- SnO_2 NF electrode was shown in Fig. 3b, where short needle-shaped branches were grown uniformly on the entire surface of the SnO_2 NF trunks. The morphology and crystal structure of the B- SnO_2 NF were characterized by TEM and HR-TEM. The TEM image in Fig. 3d shows that the branches densely and uniformly cover the entire surface of the NFs. The branches have a cone shape with an average length of ~ 26 nm and a base diameter ~ 5 nm. From the SAED pattern taken from the $\text{SnO}_2/\text{TiO}_2$ interface (inset of Fig. 3d), it can be seen that the ring SAED patterns associated with the rutile SnO_2 are observed

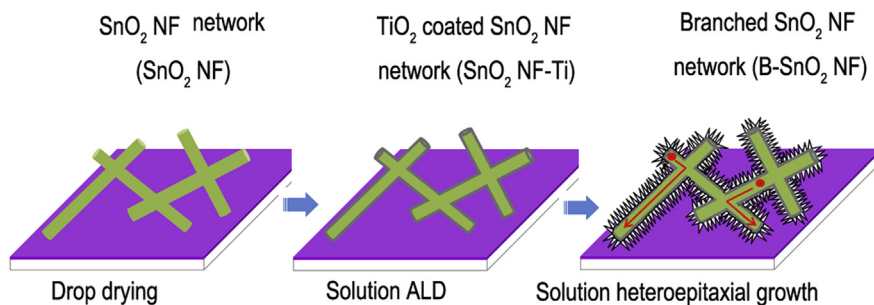


Fig. 2. Schematic description of the branched hierarchical nanostructure of TiO₂ nanoneedles on SnO₂ NF network.

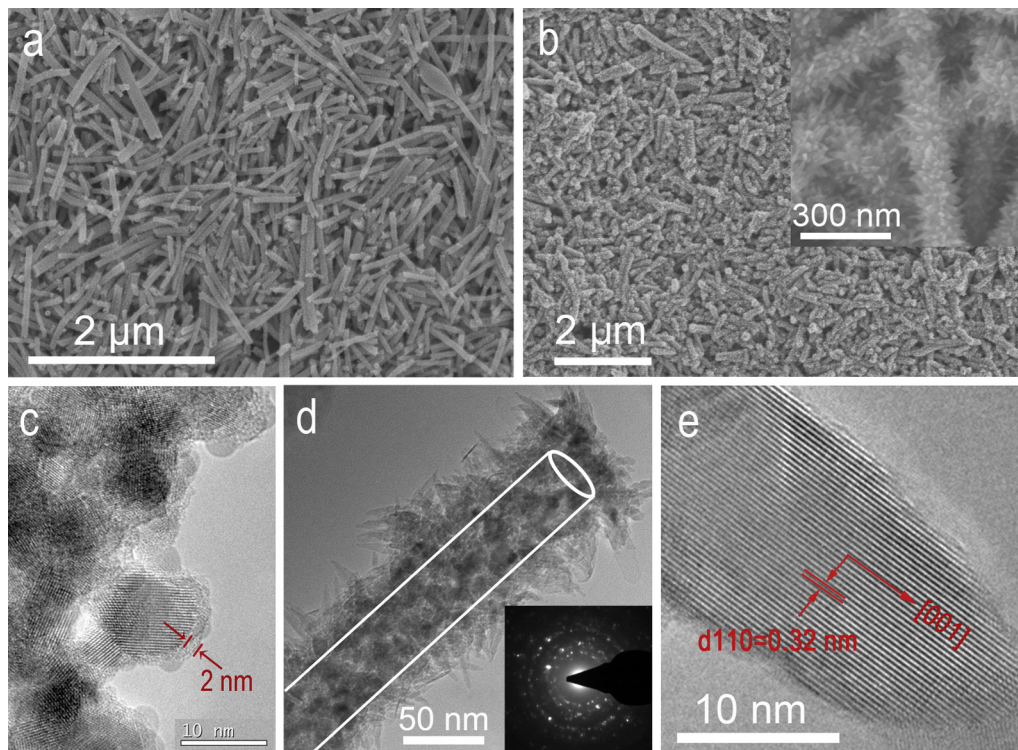


Fig. 3. FE-SEM images of the SnO₂ NF based photoanodes before (a) and after (b) growth of TiO₂ nanoneedles. Inset of (b) shows a close inspection of the branched structure. (c) HRTEM image of SnO₂ NF52-Ti showing a ~2 nm TiO₂ coating on SnO₂ NF. (d) TEM image of a single B-SnO₂ NF52. Inset shows corresponding SAED pattern taken from the SnO₂/TiO₂ interface. (e) HRTEM image of a single TiO₂ nanoneedle.

together with spot patterns from the rutile TiO₂ branches, indicating that the polycrystalline SnO₂ NF is successfully covered by radially aligned single-crystalline TiO₂ branches. A HR-TEM image of a single branch (Fig. 3e) shows well resolved lattice fringes even at the outer surface, indicating good crystallinity of the branches. The lattice constants are 0.32 nm in the parallel to the length of the branches, suggesting that the branches are single-crystalline tetragonal–rutile phase TiO₂ with a [001] growth direction, which is consistent with TiO₂ nanorods reported previously [39–41].

XRD and Raman spectroscopy were carried out on SnO₂ NF52 and B-SnO₂ NF52 film to further investigate the crystal structure of TiO₂/SnO₂ heterojunction nanostructure. As compared with SnO₂ NF52, B-SnO₂ NF52 shows two weak additional XRD peaks characteristic of rutile TiO₂ appeared at $2\theta = 27.45$ and 36.09° (JCPDS no. 34-0180), as shown in Fig. 4a. Fig. 4b compares Raman scattering spectra of SnO₂ NF52 and B-SnO₂ NF52. Pure SnO₂ shows two peaks at 472 and 628 cm⁻¹ corresponding to E_g and A_{1g} mode of SnO₂, respectively [42–44]. B-SnO₂ NF shows three distinct peaks at 239,

438 and 604 cm⁻¹, which should be assigned accordingly to B_{1g} , E_g and A_{1g} mode of rutile TiO₂, respectively. [45] Here, the 472 cm⁻¹ peak, which corresponds to Sn–O surface vibrations [44], is absent in the Raman scattering spectra of B-SnO₂ NF, indicating that the TiO₂ nanoneedles covering the entire surface of the SnO₂ NFs.

Fig. 5 compares photocurrent density–voltage (J – V) curves of DSSCs with photoanodes composed of the B-SnO₂ NF52, B-SnO₂ NF113, SnO₂ NF52-Ti, SnO₂ NF52 and TiO₂ nanoparticle (P25) under simulated solar irradiance (AM 1.5 G, 100 mW cm⁻²). The device performances are summarized in Table 1. It can be seen that the SnO₂ NF52 shows a low open-circuit voltage (V_{oc} , 0.506 V) and J_{sc} (7.04 mA cm⁻²). After a thin layer of TiO₂ was coated on the SnO₂ NF network by using the liquid atomic layer deposition method, the V_{oc} and J_{sc} increased slightly to 9.80 mA cm⁻² and 0.588 V, respectively. While after growth of the TiO₂ branches, the V_{oc} and J_{sc} increases sharply to 20.5 mA cm⁻² and 0.713 V, respectively. The cumulative increases of V_{oc} and J_{sc} give rise to an efficiency of 7.06%, which are more than four and two times larger than that of SnO₂ NF52 and SnO₂ NF52-Ti DSSC, respectively. This is because the

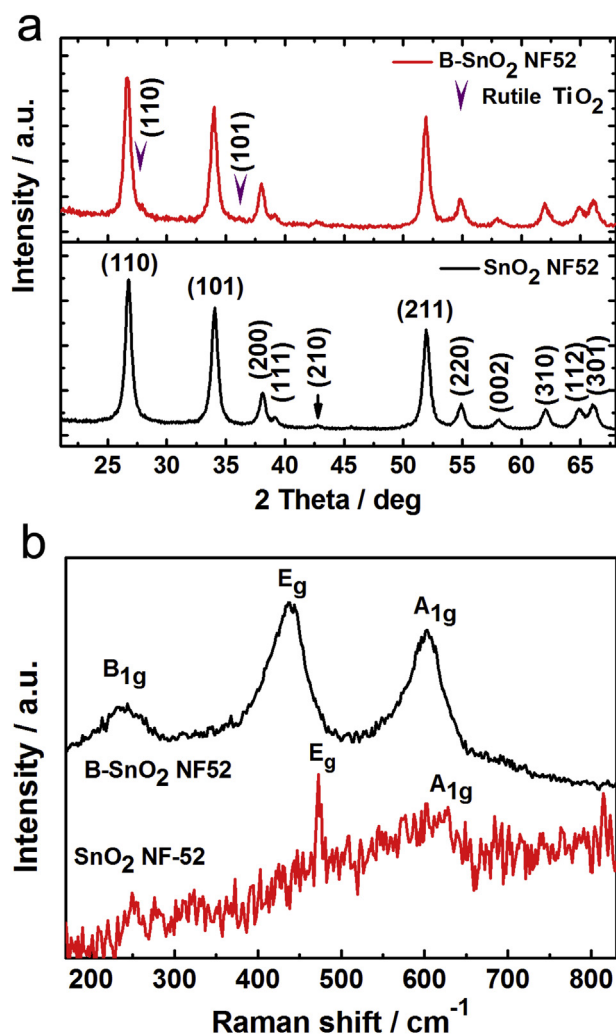


Fig. 4. (a) XRD and (b) Raman scattering spectra of B-SnO₂ NF52 and SnO₂ NF52.

conduction band of the SnO₂ was 300 mV more positive than that of TiO₂, leading to a faster interfacial electron recombination and lower trapping density [11–13,15,33,40]. The synthesis of the TiO₂ branches on the SnO₂ trunk forms a core–shell structure, which

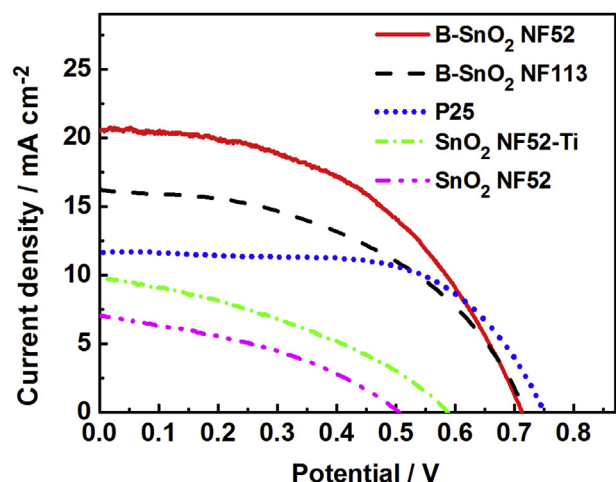


Fig. 5. J–V curves of DSSCs with the photoanode films of B-SnO₂ NF52, B-SnO₂ NF113, SnO₂ NF52-Ti, SnO₂ NF52 and TiO₂ nanoparticles (P25).

yields a surface dipole layer toward SnO₂ due to the higher iso-electric points of TiO₂ (~5–5.5) than that of SnO₂ (~4–4.4) [15,23]. Such a dipole layer can accelerate the forward electrons injection and suppress the back recombination, causing an increase in V_{oc} and J_{sc} . Moreover, since the SnO₂ network with thinner SnO₂ NFs has larger specific surface areas, and thus larger amount of adsorbed dye (Table 1), the J_{sc} of B-SnO₂ NF52 DSSC is considerably higher than that obtained from B-SnO₂ NF113 DSSC.

To reveal the effect of TiO₂ shell on interfacial characteristics of the SnO₂ based photoanode, we measured EIS spectra of B-SnO₂ NF52 and SnO₂ NF52 DSSCs. As shown in Fig. 6, in both EIS spectra, two well-defined semicircles, denote the redox reaction of I^-/I^{3-} at the Pt/electrolyte interface and the electron transfer at the semiconductor/dye/electrolyte interface according to recent analysis on the EIS spectra of DSSCs, were observed in the region of 100, 000–1000 Hz, 1000–1 Hz, respectively. The lifetime of the electrons in the oxide film (τ_n) can be estimated according to the relation $\tau_n = 1/2\pi f_{max}$, where f_{max} is the maximum frequency of the mid-frequency peak in the bode phase plots. The f_{max} value for the B-SnO₂ NF52 is ~2.86 Hz, much smaller than the values for SnO₂ NF52 (~8.32 Hz), indicating that electron recombination on SnO₂/dye/electrolyte interface is effectively suppressed.

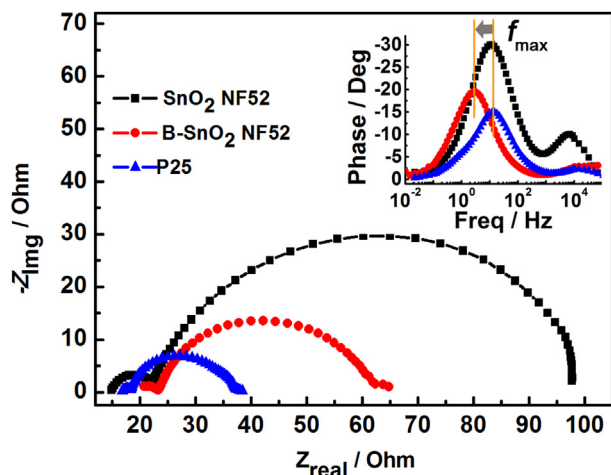
The distinct photovoltaic behavior of the B-SnO₂ NF52 is its large J_{sc} (20.5 mA cm⁻²) compared with the commonly used P25 photoanode (11.7 mA cm⁻²), even though the amount of dye molecules adsorbed to the B-SnO₂ NF52 (0.984×10^{-7} mol cm⁻¹) is less than that of P25 (1.06×10^{-7} mol cm⁻¹). This result is in accordance with the previous reports [11,15,16,28], indicating excellent charge transport and recombination property of the SnO₂–TiO₂ based DSSCs. One reason for the increase of J_{sc} is the low degree of charge recombination loss associated with the formation of core–shell structure. The electron lifetime in B-SnO₂ NF52 ($\tau_n = 0.056$ s) film is much longer than that in P25 film ($\tau_n = 0.012$ s), Fig. 7, suggesting that the back electron transfer is much slower in B-SnO₂ NF52 than in P25 photoanode. Another reason is due to the direct pathway for electron transport associated with construction of SnO₂ NF network, resulting in faster electron transport and charge collection efficiency. The charge-collection properties of the DSSCs are discussed in terms of the charge-collection time (τ_c), which considers the differences in the time scales of charge transport and recombination [26,40,46]. The τ_c was obtained by first-order decay kinetics fitting of the transient photocurrent profile using a homogeneous light (532 nm) in a short-circuit condition, as described in the Supporting information (Fig. S3). As shown in Fig. 7, the τ_c of the B-SnO₂ NF52 DSSC is smaller than that of P25 DSSC for the entire range of J_{sc} , the difference becoming larger as the J_{sc} decreases. Because electron diffusion within a nanoparticle network film is determined by trapping/detrapping events, τ_c of P25 DSSCs depends on light intensity [15,47]. Whereas the B-SnO₂ NF52 DSSC shows negligible dependence of τ_c on the light intensity, indicating excellent electron transport property of the SnO₂ NF based photoanodes.

Open-circuit voltage-decay (OCVD) technique can provide additional information and deeper understanding on the differences in electron transport and recombination property between SnO₂ NF network DSSCs and TiO₂ nanoparticle DSSCs. The OCVD gives a continuous reading of the electron lifetime (τ_n) as a function of V_{oc} at high-voltage resolution, as described in the Supporting information (Fig. S4). As shown in Fig. 8, The shape of the τ_n – V_{oc} curve for P25 shows a dependence on the quasi-Fermi level, indicating a trap-assisted conduction mechanism, which are in accordance with that of nanoparticles [15,48–50]. The deviation of the τ_n – V_{oc} curve for P25 from linear suggests a high recombination rate constant. While the τ_n – V_{oc} curves for the SnO₂ NF network based DSSCs, even the pure SnO₂ NF DSSC, show a weak dependence on

Table 1

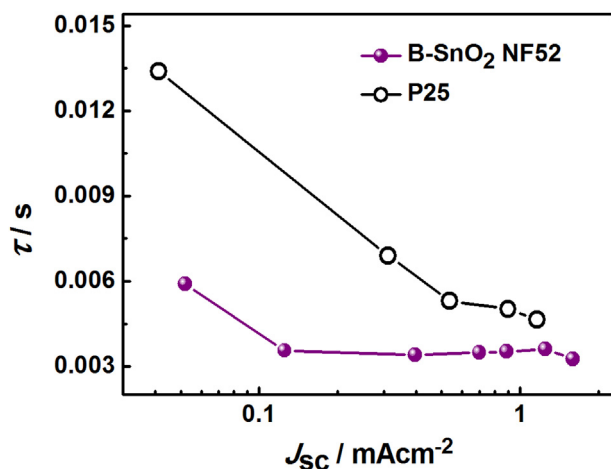
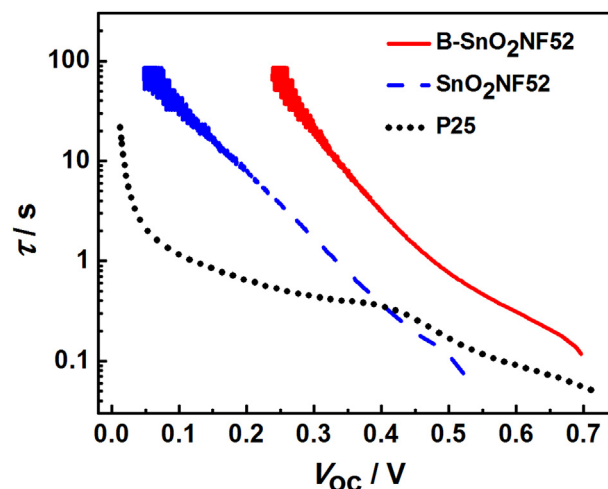
Comparison of short-circuit photocurrent density (J_{sc}), open-circuit photovoltage (V_{oc}), fill factor (FF) and power conversion efficiency (PCE) along with R_s , f_{max} and the amount of adsorbed dye N719 for the DSSCs with B-SnO₂ NF-52, B-SnO₂ NF-113, SnO₂ NF-52-Ti, SnO₂ NF-52 and P25 films as photoanodes.

R	J_{sc} [mA cm ⁻²]	V_{oc} [V]	FF	PCE [%]	R_s [Ω]	f_{max} [Hz]	Adsorbed dye [×10 ⁻⁷ mol cm ⁻¹]
B-SnO ₂ NF-52	20.5	0.713	0.483	7.06	20.4	2.86	0.984
B-SnO ₂ NF-113	16.5	0.720	0.469	5.57	—	—	0.603
P25	11.7	0.748	0.576	5.04	16.9	13.3	1.06
SnO ₂ NF-52-Ti	9.80	0.588	0.366	2.11	—	—	—
SnO ₂ NF-52	7.04	0.506	0.378	1.34	15.0	8.32	—

Fig. 6. EIS of DSSCs with the photoanode films of B-SnO₂ NF52, SnO₂ NF52 and P25.

the quasi-Fermi level, indicating fast electron transport in SnO₂ NF network and low degree of electron recombination at the SnO₂–TiO₂/electrolyte interface. In conclusion, the slower electron recombination and faster electron transport in the B-SnO₂ NF52 DSSC contributed to the 76% increase in photocurrent generation compared to P25 DSSC.

It is noteworthy that the SnO₂–TiO₂ based DSSC have a low fill factor (FF) as compared to P25. FF is usually governed by the series resistance (R_s) which can be measured by EIS. As shown in Table 1, after growth of TiO₂ nanoneedles on SnO₂ network, the R_s

Fig. 7. Charge-collection time (τ_c) calculated from photocurrent decay curves of B-SnO₂ NF52 and P25 DSSCs as a function of J_{sc} .Fig. 8. Electron lifetime as a function of V_{oc} for DSSCs with the photoanode films of B-SnO₂ NF52, SnO₂ NF52 and P25.

increased from 15.0 to 20.4 Ω. This is due to the occurrence of cracks in the SnO₂ NF network resulted from the growth of TiO₂, leading to increase of the contact resistance between the semiconductor film and FTO layer. However, the B-SnO₂ NF52 DSSC still exhibited a high J_{sc} and PCE value, despite its low FF. We expect that the photovoltaic performance could be further increased by reducing the contact resistance between the semiconductor film and FTO layer, such as using graphene oxide as auxiliary binder to release stress [51].

4. Conclusions

In summary, we have synthesized five nanostructured films made of B-SnO₂ NF52, B-SnO₂ NF113, SnO₂ NF52-Ti, SnO₂ NF52 and P25, and compared their photovoltaic performances. Under an illumination of one sun condition (AM 1.5 G, 100 mW cm⁻²), the PCE for B-SnO₂ NF52 is up to 7.06%, increased by 26% and 40% compared to B-SnO₂ NF113 (5.57%) and P25 (5.04%), respectively, and more than five times as large as SnO₂ NF52 (1.34%). It is demonstrated that this novel nanostructure simultaneously offers a low degree of charge recombination and a fast electron transport in DSSCs. The branched hierarchical nanostructures of TiO₂ nanoneedles on ultrafine SnO₂ nanofiber network given herein provides a new approach to achieve those conflicting requirements simultaneously and may facilitate the development of DSSCs. In addition, this structure is extendable to other applications based on photoelectrochemical effect, such as photoelectrochemical hydrogen production, and could improve their efficiencies as well.

Acknowledgments

This work was financially supported by the National Natural Science Foundation of China (No. 61176058 and 51302122) and Science and Technology Planning Project of Sichuan Province, China (No. 2014JY0094).

Appendix A. Supplementary data

Supplementary data related to this article can be found at <http://dx.doi.org/10.1016/j.jpowsour.2014.04.059>.

References

- [1] B. O'Regan, M. Grätzel, *Nature* 353 (1991) 737.
- [2] C. Longo, M.-A. De Paoli, J. Braz. Chem. Soc. 14 (2003) 898–901.
- [3] J.-H. Yum, S.-J. Moon, C.S. Karthikeyan, H. Wietasch, M. Thelakkat, S.M. Zakeeruddin, M.K. Nazeeruddin, M. Grätzel, *Nano Energy* 1 (2012) 6–12.
- [4] A. Yella, H.-W. Lee, H.N. Tsao, C. Yi, A.K. Chandiran, M.K. Nazeeruddin, E.W.-G. Diao, C.-Y. Yeh, S.M. Zakeeruddin, M. Grätzel, *Science* 334 (2011) 629–634.
- [5] Horim Lee, Daesub Hwang, Seong Mu Jo, Dongho Kim, Yongsok Seo, D.Y. Kim, *ACS Appl. Mater. Interfaces* 4 (2012) 3308–3315.
- [6] S. Ito, P. Chen, P. Comte, M.K. Nazeeruddin, P. Liska, P. Péchy, M. Grätzel, *Prog. Photovoltaics Res. Appl.* 15 (2007) 603–612.
- [7] M. Fujimoto, T. Kado, W. Takashima, K. Kaneto, S. Hayase, *J. Electrochem. Soc.* 153 (2006) A826–A829.
- [8] D. Hwang, H. Lee, S.-Y. Jang, S.M. Jo, D. Kim, Y. Seo, D.Y. Kim, *ACS Appl. Mater. Interfaces* 3 (2011) 2719–2725.
- [9] Y. Zhang, L. Wu, E. Xie, H. Duan, W. Han, J. Zhao, *J. Power Sources* 189 (2009) 1256–1263.
- [10] X. Li, Y. Zhang, Z. Zhang, J. Zhou, J. Song, B. Lu, E. Xie, W. Lan, *J. Power Sources* 196 (2011) 1639.
- [11] J. Qian, P. Liu, Y. Xiao, Y. Jiang, Y. Cao, X. Ai, H. Yang, *Adv. Mater.* 21 (2009) 3663–3667.
- [12] S. Chappel, S.-G. Chen, A. Zaban, *Langmuir* 18 (2002) 3336–3342.
- [13] H.J. Snaith, C. Ducati, *Nano Lett.* 10 (2010) 1259–1265.
- [14] K.-N. Li, Y.-F. Wang, Y.-F. Xu, H.-Y. Chen, C.-Y. Su, D.-B. Kuang, *ACS Appl. Mater. Interfaces* 5 (2013) 5105–5111.
- [15] C. Gao, X. Li, B. Lu, L. Chen, Y. Wang, F. Teng, J. Wang, Z. Zhang, X. Pan, E. Xie, *Nanoscale* 4 (2012) 3475–3481.
- [16] M. Peng, X. Cai, Y. Fu, X. Yu, S. Liu, B. Deng, K. Hany, D. Zou, *J. Power Sources* 247 (2014) 249–255.
- [17] Y.J. Kim, M.H. Lee, H.J. Kim, G. Lim, Y.S. Choi, N.-G. Park, K. Kim, W.I. Lee, *Adv. Mater.* 21 (2009) 3668–3673.
- [18] R. Gao, Z. Liang, J. Tian, Q. Zhang, L. Wang, G. Cao, *Nano Energy* 2 (2013) 40–48.
- [19] C. Gao, X. Li, Y. Wang, L. Chen, X. Pan, Z. Zhang, E. Xie, *J. Power Sources* 239 (2013) 458–465.
- [20] B.-h. Li, Y.-w. Tang, L.-j. Luo, T. Xiao, D.-w. Li, X.-y. Hu, M. Yuan, *Appl. Surf. Sci.* 257 (2010) 197–202.
- [21] D.W. Kim, S.S. Shin, S. Lee, I.S. Cho, D.H. Kim, C.W. Lee, H.S. Jung, K.S. Hong, *ChemSusChem* 6 (2013) 449–454.
- [22] S.S. Shin, J.S. Kim, J.H. Suk, K.D. Lee, D.W. Kim, J.H. Park, I.S. Cho, K.S. Hong, J.Y. Kim, *ACS Nano* 7 (2013) 1027–1035.
- [23] Q. Zhang, G. Cao, *Nano Today* 6 (2011) 91–109.
- [24] L. Li, T. Zhai, Y. Bando, D. Golberg, *Nano Energy* 1 (2012) 91–106.
- [25] G.K. Mor, O.K. Varghese, M. Paulose, K. Shankar, C.A. Grimes, *Sol. Energy Mater. Sol. Cells* 90 (2006) 2011–2075.
- [26] J.H. Noh, H.S. Han, S. Lee, J.Y. Kim, K.S. Hong, G.-S. Han, H. Shin, H.S. Jung, *Adv. Energy Mater.* 1 (2011) 829–835.
- [27] K. Park, Q. Zhang, B.B. Garcia, X. Zhou, Y.-H. Jeong, G. Cao, *Adv. Mater.* 22 (2010) 2329–2332.
- [28] H. Song, K.-H. Lee, H. Jeong, S.H. Um, G.-S. Han, H.S. Jung, G.Y. Jung, *Nanoscale* 5 (2013) 1188–1194.
- [29] C.G. Fonstad, R.H. Rediker, *J. Appl. Phys.* 42 (1971) 2911–2918.
- [30] R.G. Breckenridge, W.R. Hosler, *Phys. Rev.* 91 (1953) 793–802.
- [31] A.N.M. Green, E. Palomares, S.A. Haque, J.M. Kroon, J.R. Durrant, *J. Phys. Chem. B* 109 (2005) 12525–12533.
- [32] V. Ganapathy, B. Karunakaran, S.W. Rhee, *J. Power Sources* 195 (2010) 5138–5143.
- [33] S.H. Ahn, D.J. Kim, W.S. Chi, J.H. Kim, *Adv. Mater.* 25 (2013) 4893–4897.
- [34] N.K. Huu, D.-Y. Son, I.-H. Jang, C.-R. Lee, N.-G. Park, *ACS Appl. Mater. Interfaces* 5 (2013) 1038–1043.
- [35] N.G. Park, M.G. Kang, K.M. Kim, K.S. Ryu, S.H. Chang, D.K. Kim, J. van de Lagemaat, K.D. Benkstein, A.J. Frank, *Langmuir* 20 (2004) 4246–4253.
- [36] G. Shang, J. Wu, M. Huang, J. Lin, Z. Lan, Y. Huang, L. Fan, *J. Phys. Chem. C* 116 (2012) 20140–20145.
- [37] Y.X.D. Li, *Adv. Mater.* 16 (2004) 1151–1170.
- [38] B. Lu, X. Guo, Z. Bao, X. Li, Y. Liu, C. Zhu, Y. Wang, E. Xie, *Nanoscale* 3 (2011) 2145–2149.
- [39] I.S. Cho, Z. Chen, A.J. Forman, D.R. Kim, P.M. Rao, T.F. Jaramillo, X. Zheng, *Nano Lett.* 11 (2011) 4978–4984.
- [40] X. Li, C. Gao, H. Duan, B. Lu, Y. Wang, L. Chen, Z. Zhang, X. Pan, E. Xie, *Small* 9 (2013) 2005–2011.
- [41] Y. Xie, L. Wei, G. Wei, Q. Li, D. Wang, Y. Chen, S. Yan, G. Liu, L. Mei, J. Jiao, *Nanoscale Res. Lett.* 8 (2013) 188.
- [42] K. McGuire, Z.W. Pan, Z.L. Wang, D. Milkie, J. Menendez, A.M. Rao, *J. Nanosci. Nanotechnol.* 2 (2002) 499–502.
- [43] N. Dharmaraj, C.H. Kim, K.W. Kim, H.Y. Kim, E.K. Suh, *Spectrochim. Acta A* 64 (2006) 136–140.
- [44] S.S. Bhande, G.A. Taur, A.V. Shaikh, O.-S. Joo, M.-M. Sung, R.S. Mane, A.V. Ghule, S.-H. Han, *Mater. Lett.* 79 (2012) 29–31.
- [45] W. Ma, Z. Lu, M. Zhang, *Appl. Phys. A Mater. Sci. Process.* 66 (1998) 621–627.
- [46] M. Grätzel, *Inorg. Chem.* 44 (2005) 6841–6851.
- [47] J. van de Lagemaat, A.J. Frank, *J. Phys. Chem. B* 105 (2001) 11194–11205.
- [48] J. Bisquert, A. Zaban, M. Greenshtein, I. Mora-Seró, *J. Am. Chem. Soc.* 126 (2004) 13550–13559.
- [49] X. Li, C. Gao, J. Wang, B. Lu, W. Chen, J. Song, S. Zhang, Z. Zhang, X. Pan, E. Xie, *J. Power Sources* 214 (2012) 244–250.
- [50] P.S. Archana, R. Jose, C. Vijila, S. Ramakrishna, *J. Phys. Chem. C* 113 (2009) 21538–21542.
- [51] C.Y. Neo, J. Ouyang, *J. Power Sources* 222 (2013) 161–168.